Solar Phys (2011) 273:179–203
DOI 10.1007/s11207-011-9858-7

Comparison of Observations at ACE and *Ulysses* with Enlil Model Results: Stream Interaction Regions During Carrington Rotations 2016 – 2018

L.K. Jian · C.T. Russell · J.G. Luhmann · P.J. MacNeice · D. Odstrcil · P. Riley · J.A. Linker · R.M. Skoug · J.T. Steinberg

Received: 7 March 2011 / Accepted: 26 August 2011 / Published online: 5 October 2011

Abstract During the latitudinal alignment in 2004, ACE and *Ulysses* encountered two stream interaction regions (SIRs) each Carrington rotation from 2016 to 2018, at 1 and 5.4 AU, respectively. More SIR-driven shocks were observed at 5.4 AU than at 1 AU. Three small SIRs at 1 AU merged to form a strong SIR at 5.4 AU. We compare the Enlil model results with spacecraft observations from four aspects: *i*) the accuracy of the latest versions of models (WSA v2.2 and Enlil v2.7) *vs.* old versions (WSA v1.6 and Enlil v2.6), *ii*) the sensitivity to different solar magnetograms (MWO *vs.* NSO), *iii*) the sensitivity to different coronal models (WSA *vs.* MAS), *iv*) the predictive capability at 1 AU *vs.* 5.4 AU. We find the models can capture field sector boundaries with some time offset. Although the new versions have improved the SIR timing prediction, the time offset can be up to two days at 1 AU and four days at 5.4 AU. The models cannot capture some small-scale structures, including shocks and small SIRs at 1 AU. For SIRs, the temperature and total pressure are often underestimated, while the density compression is overestimated. For slow wind, the density is usually overestimated, while the temperature, magnetic field, and total pressure are often underestimated. The new versions have improved the prediction of the speed and density, but they need more robust scaling factors for magnetic field. The Enlil model results are very sensitive to different solar magnetograms and coronal models. It is hard to determine which magnetogram-coronal model combination is superior to others. Higher-resolution solar and

L.K. Jian (✉) · C.T. Russell
Institute of Geophysics and Planetary Physics, University of California, Los Angeles, CA 90095, USA
e-mail: jlan@igpp.ucla.edu

J.G. Luhmann
Space Sciences Laboratory, University of California, Berkeley, CA 94720, USA

P.J. MacNeice · D. Odstrcil
NASA, Goddard Space Flight Center, Code 674, Greenbelt, MD 20771, USA

P. Riley · J.A. Linker
Predictive Science, Inc., San Diego, CA 92121, USA

R.M. Skoug · J.T. Steinberg
Space Science and Applications, Los Alamos National Laboratory, Los Alamos, NM 87545, USA

coronal observations, a mission closer to the Sun, together with simulations of greater resolution and added physics, are ways to make progress for the solar wind modeling.

Keywords Coronal model · Corotating interaction region · Heliospheric model · Radial evolution · Solar wind · Space weather

1. Introduction

Stream interaction regions (SIRs) are formed when fast solar wind overtakes and compresses preceding slow solar wind. In contrast to the interplanetary CMEs (ICMEs), SIRs persist throughout a solar cycle and are the predominant solar wind structure in the declining phase and around solar minimum. When solar conditions do not change substantially over a few solar rotations, SIRs can last for several solar rotations and are called corotating interaction regions or CIRs (Smith and Wolfe, 1976). The high-speed streams at the SIRs contribute about 30% of geomagnetic activity at solar maximum and about 70% outside of solar maximum (Richardson, Cliver, and Cane, 2000). Therefore, being able to capture these SIRs is an important element of heliospheric modeling and the foundation of successful space weather forecasting. Our statistical work on SIRs at multiple heliocentric distances (Jian *et al.*, 2006, 2008a, 2008b, 2008c) prepares us for examining several SIRs at 1 and 5.4 AU in depth here to evaluate the capability of latest models to reproduce these SIRs and their radial variations.

1.1. Observations

As the first spacecraft to study the Sun and solar wind at nearly all latitudes, *Ulysses* orbited the Sun in a trajectory highly inclined to the ecliptic plane (Wenzel *et al.*, 1989). With a period of 6.2 years, *Ulysses* accomplished nearly three complete orbits in its lifetime and made three aphelion passes at 5.4 AU in February 1992, April 1998, and June 2004. The coverage of contemporary 1-AU solar wind observations was poor during *Ulysses*' first aphelion pass. But during the second and third aphelion passes, the *Advanced Composition Explorer* (ACE) provided continuous solar wind monitoring at 1 AU, enabling us to study the radial evolution of individual SIR events. However, not every latitudinal alignment during the two aphelion passes was appropriate. Sometimes the solar wind structure was too complicated and varied dramatically from 1 to 5.4 AU, especially during periods of strong solar activity; at other times no clearly identifiable events were observed.

In our earlier surveys of SIRs from ACE and *Ulysses* (Jian *et al.*, 2006, 2008b), no well-defined recurring SIRs occurred at both spacecraft during *Ulysses'* aphelion pass in April 1998, probably because it was in the rising phase of solar cycle 23 and some transient events occurred on the Sun. In fact, the ICME whose radial evolution was studied by Skoug *et al.* (2000) as well as Du, Wang, and Hu (2007) occurred in the second aphelion pass, when ACE and *Ulysses* were also nearly in longitudinal alignment. In contrast, the aphelion pass in June 2004 fell in the declining phase of solar cycle 23. Both ACE and *Ulysses* observed several SIRs during this interval. For this study, we choose the two well-defined SIRs during Carrington rotations (CRs) 2016 – 2018. They have the following SIR signatures as required in Jian *et al.* (2006, 2008b): an overall increase of solar wind speed, solar wind velocity deflection, an increase and then decrease of proton number density, an increase of proton temperature, a compression of magnetic field, and a pile-up of total pressure P_t (the sum of magnetic and plasma thermal pressures).

From our statistics of SIRs at 1 AU over 15 years (Jian, Russell, and Luhmann, 2011), only about 21% of SIRs have sharp and simultaneous variations of density, temperature,

and speed increase (within a 10-min window), as characteristic of the boundary between slow and fast streams. Hence, we define the stream interface at the peak P_t where the forces pushing toward the two sides are balanced (Jian *et al.*, 2006). Such a definition can be equally applicable to many SIRs. Considering SIRs have variable durations, in order to focus on the stream interaction, we use the stream interface time rather than the SIR start time to assess the timing of the models. Because ACE and *Ulysses* were not aligned in longitude during this aphelion pass, both radial propagation time and solar rotation time need to be considered. The time shift from ACE (1) to *Ulysses* (2) would be

$$\Delta t = t_2 - t_1 = (\varphi_2 - \varphi_1)/\omega_{\mathrm{Sun}} + (r_2 - r_1)/v_{\mathrm{sw}}, \tag{1}$$

where φ denotes the longitude, ω_{Sun} as the solar rotation angular speed, r as the heliocentric distance, and v_{sw} being the solar wind speed.

1.2. Models

The Community Coordinated Modeling Center (CCMC) is a multi-agency partnership situated at the Goddard Space Flight Center of NASA. Through the effort of model developers and CCMC staff over years, several solar and heliospheric models have been installed and used for runs-on-request at the CCMC. In order to compare with the solar wind observations at both 1 and 5.4 AU, we use the Enlil model, currently the only heliospheric model running beyond 5 AU at CCMC. Because the heliospheric model is designed for supersonic, super-Alfvénic, and low-β plasma, it needs inner boundary conditions from the coronal portion of either the Wang–Sheeley–Arge (WSA) model or the Magnetohydrodynamics-Around-a-Sphere (MAS) model.

The Enlil model is a time-dependent 3D MHD heliospheric model developed by Dusan Odstrcil and his colleague. This model solves equations for plasma mass, momentum, energy density, and magnetic field (Odstrcil *et al.*, 2002; Odstrcil, 2003), using the explicit finite difference Total-Variation-Diminishing Lax–Friedrich (TVDLF) algorithm on a non-staggered numerical grid (Toth and Odstrcil, 1996). The algorithm uses no explicit artificial diffusion and produces second-order accuracy away from shocks and discontinuities, while simultaneously providing the stability that ensures non-oscillatory solutions. The inner boundary is located at either 21.5 solar radii (R_s) for WSA coronal model as input or 30 R_s for MAS coronal model as input, both beyond the critical point of the solar wind. At the inner boundary, the solar rotation is added by imparting a corotational magnetic field component. The outer boundary of the Enlil model can be adjusted to include planets or spacecraft of interest, with options of 2 and 10 AU available at the CCMC. In order to obtain results at 5.4 AU, we had to run the model all the way to 10 AU. The CCMC plans to add one more option of 5.5 or 6 AU, which will maximize the usage of the grids and be useful to provide the solar wind condition for the investigation of Jupiter.

For the robustness of runs at the CCMC and for matching with typical interplanetary magnetic field (IMF) values at 1 AU, the old version 2.6 of the Enlil model at CCMC uses free field strength at the inner boundary and tracks the location of the heliospheric current sheet (HCS). Because the solar wind kinetic energy is significantly larger than the thermal or magnetic energy in the domain of the heliospheric model, the solar wind evolution in the simulation should not be affected much by the change of the field strength. However, the old version obtained poor spiral shapes for slow wind because the wind was assumed fast everywhere when computing the azimuthal field correction. The latest version 2.7 of the Enlil model uses the variable field from the synoptic maps and coronal models, so it has

significantly better IMF tracing. The azimuthal field setting is dependent on the local wind speed given by WSA model (not yet changed for the MAS coronal model), so the spiral shape problem is fixed for the WSA-Enlil run. However, the free parameters for Enlil v2.7 are not pre-calibrated on a large number of CRs as was the previous v2.6 and they require tuning for specific cases especially for magnetic field. A scaling factor of 3 – 4 depending on the solar observatory and coronal model is needed for the solar minimum 23/24 to match the IMF observations.

The Enlil model does not currently include corrections for any additional solar wind physics en route to 10 AU such as shock-related heating or interstellar pickup ion effects, which may become important between 5 and 10 AU. From the comparison in Section 2, we can see the temperature is often underestimated even at 1 AU. Additional solar wind heating is needed for both coronal and heliospheric models. We choose the highest-resolution grid available, which is a uniform mesh of $1280 \times 45 \times 180$ (radial $\times$ latitude $\times$ longitude) grid points for the 10-AU and 360°-longitude heliosphere covering $\pm 44°$ in helio-latitude, to concentrate grid points in the low-latitude region near the ecliptic plane. In other words, the spatial resolution of the Enlil model for our runs is approximately 0.0078 AU (about 1.66 R_s) in radial distance, 2° in helio-latitude and helio-longitude. Output options are available at CCMC to obtain results calculated at Earth, *Ulysses*, and other planets and spacecraft. This is a function added in 2010, and the trajectories of these objects are automatically taken into account.

The WSA coronal model combines a magnetostatic potential-field source surface (PFSS) model (Altschuler and Newkirk, 1969; Schatten, Wilcox, and Ness, 1969) and the Schatten current sheet model (Schatten, 1971). From the photosphere to the hypothetical sphere (the "source surface") where the solar wind takes over at 2.5 R_s, the PFSS approximation is used and the magnetic field lines are constrained to be radial. From 2.5 to 21.5 R_s, the Schatten current sheet model is incorporated in order to obtain a more realistic magnetic field configuration of the outer corona with the field lines diverging toward the current sheet (Arge *et al.*, 2004). This model uses an improved Wang and Sheeley empirical relationship (Wang and Sheeley, 1990a, 1990b; Arge and Pizzo, 2000; Arge *et al.*, 2002) to derive the solar wind speed at 21.5 R_s based on the relative expansion of the magnetic field lines from 1 to 21.5 R_s as well as the distance from coronal hole boundaries. Assuming momentum-flux conservation and thermal-pressure balance, the WSA model also derives the density and temperature for the coronal region. Although the WSA model is an empirical model, it turns out to be very efficient and relatively accurate. Due to the current insufficient understanding of coronal physics, the WSA model is still widely used in the community and routinely used for space weather forecasting. There are some subtle tuning differences in its new version 2.2 in comparison with the previous v1.6.

The MAS coronal model is a time-dependent 3D MHD model covering 1 – 30 R_s developed by Predictive Science, Inc. (Riley, Linker, and Mikić, 2001; Riley *et al.*, 2001). Based on solar synoptic maps, MAS first uses a potential field model and a Parker solar wind solution (Parker, 1963) to determine the initial plasma and magnetic field parameters, and then solves the Maxwell equations as well as the continuity, momentum, and energy equations to obtain a steady-state MHD solution. Because the MAS model at CCMC uses a simple polytropic energy equation, the numerically-derived fast wind in the solution is too slow (Riley, Linker, and Mikić, 2001). Some *ad hoc* corrections for the expected velocity dependent on the distance from open field line boundaries are added at 30 R_s (Riley, Linker, and Mikić, 2001; Riley *et al.*, 2001). These corrections are consistent with the well-accepted views on the different origins of slow and fast wind. Similar to the WSA model, the density and temperature are obtained based on the conservation of momentum flux and the balance

of thermal pressure. To support the Enlil v2.7, the substantive difference from MAS v3.5 to the present v4.2.r45 is that the code is changed from serial to parallelized, but the physics of MAS model is essentially unchanged (Janvier Wijaya, personal communication in 2011).

As space weather forecasting becomes more desirable and even necessary for space-related applications including the support of missions, it is essential to evaluate quantitatively how well the present models describe the solar wind structure. Following the development of the models, several comparative studies of the observations and models have been conducted by a third party rather than model developers.

Owens *et al.* (2008) compared the near-Earth observations with the results from WSA heliospheric model, WSA-Enlil, and MAS-Enlil models over 1995 – 2002, and found the WSA heliospheric model gave the best forecast of solar wind speed at 1 AU, and the other two models could capture dynamic effects at SIRs better. Using high-speed enhancements as significant features in the solar wind time series, Owens *et al.* (2008) found that the WSA heliospheric model and MAS-Enlil model had a similar accuracy of predicting the event occurrence, much better than WSA-Enlil model, which lacked the variability of solar wind speed especially during 1995 and 1996. They concluded the empirical WSA model was relatively mature and the other two physics-based models had the potential to surpass the predictive capability of empirical schemes.

Lee *et al.* (2009) compared the solar wind observations at 1 AU with the Enlil model version 2.3a during January 2003 – January 2006, the declining phase of solar cycle 23. They found an overall agreement between model results and observations for the general large-scale solar wind structures and trends. They also noted that MAS-Enlil model generated more high-density intervals, more low-speed and high-speed intervals than WSA-Enlil model.

However, the long-term statistical comparisons may bury the details of how well models work for individual events. For example, the timing is earlier for some events and later for others, resulting in no systematic offset in statistical sense (Owens *et al.*, 2005), but users have no warning of how far off the timing can be. So in this study, we focus on SIRs during three CRs with no ICME encounters and quantify various aspects of the predictive capabilities of the models. In addition, after nearly 4-years use of v2.3a, version 2.6 of Enlil model became available at CCMC in early 2010 and version 2.7 was open to general users in May 2011. It is thus timely to evaluate the new version of Enlil model. Such assessments can help improve the models' capability to describe solar wind conditions during times of quiet solar activity and provide the background conditions for transient events such as CMEs.

The inputs to both the WSA and MAS coronal models at CCMC are the full-CR synoptic maps derived from photospheric magnetograms, which are ground-based or near-Earth spacecraft line-of-sight (LOS) observations. These maps are different from the daily updated synoptic maps which do not have specific start and end dates. Although the daily updated map incorporates the most recent observations, it is much more sensitive to the quality of individual magnetograms and susceptible to projection effects (Arge and Pizzo, 2000). In addition, because the Enlil model generates a stationary solar wind solution for a given synoptic map, the 1-AU results have an about 4-day phase lag due to the solar wind propagation time. This can cause poor correspondence between the model results and the spacecraft observations for the first few days of each CR (MacNeice, 2009).

At CCMC, there are currently three sources of solar magnetograms for the WSA model: Mount Wilson Observatory, MWO (Ulrich *et al.*, 2002), National Solar Observatory (NSO) at Kitt Peak in Arizona (Pierce, 1969), or Global Oscillation Network Group (GONG) Observatory (Harvey *et al.*, 1996; Leibacher, 1999). Since the use of the GONG data is still in

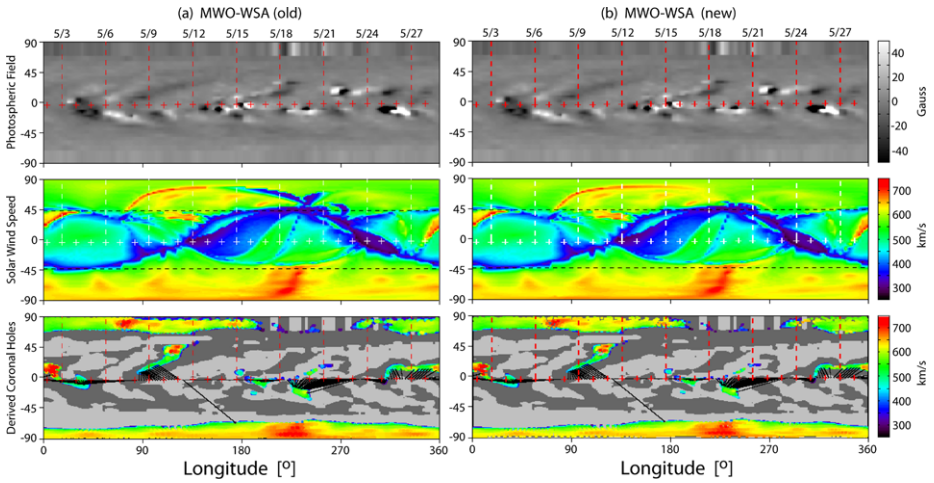

Figure 1 The MWO photospheric magnetograph (same for left and right) and the WSA coronal model results (left from old version 1.6, right from new version 2.2) for CR 2016. The panels from top to bottom: the MWO photospheric magnetograph; the derived solar wind speed at 21.5 R_S ($\approx$0.1 AU); the derived coronal hole areas with the solid black lines connecting the outer coronal boundary at 21.5 R_S and its source regions at the photosphere. In the middle panel, the two dashed black lines mark the latitudinal range covered in Figure 2. In the bottom panel, the colored dots represent photospheric footpoints of the open field lines. The areas shaded light (or dark) gray denote closed field lines with positive (or negative) radial magnetic field in the photosphere. The color scale indicates the solar wind speed at 21.5 R_S (related to the expansion factor, see Arge *et al.* (2004) and references therein) associated with the flux tubes. In all these panels, the + symbol marks the daily position of the sub-Earth point on the Sun, and the time sequence is from left to right.

trial mode, we use MWO or NSO magnetograms as the WSA model input. Although the CCMC has plans to add more magnetogram options for the MAS model, the MAS model only uses NSO magnetogram at this writing. Because the NSO synoptic map is not available for CR 2016, we only run the WSA-Enlil model for this CR. For CRs 2017 and 2018, we have all three runs: MWO with WSA corona/Enlil (MWO-WSA-Enlil), and NSO with WSA corona/Enlil (NSO-WSA-Enlil), and NSO with MAS corona/Enlil (NSO-MAS-Enlil). Comparing the MWO-WSA-Enlil and NSO-WSA-Enlil runs, we analyze the effect of different solar magnetogram input on the WSA-Enlil model results. Comparing the NSO-WSA-Enlil and NSO-MAS-Enlil runs, we can evaluate the effect of different coronal models on the Enlil results. Only the MWO synoptic map is available for CR 2019 and the latitudinal offset between ACE and *Ulysses* is more than 10° during CR 2019, thus we only examine CRs 2016 – 2018.

2. Comparison Between Observations and Model Results

During May – July 2004, *Ulysses* was close to the ecliptic plane at about 5.4 AU, at nearly the same helio-latitude as ACE. At both spacecraft, two SIRs recurred during CRs 2016 – 2018, and their features varied from one CR to another. From Equation (1), we determine the expected time shift from ACE to *Ulysses* and track the same event. The estimated dipole tilt for this period is about 50° from Wilcox Solar Observatory computation, typical for a declining phase of the solar cycle. Comparing the solar wind distribution derived from the MWO-WSA model in Figures 1, 4, and 7, we can see that from CR 2016 to 2018, the neutral

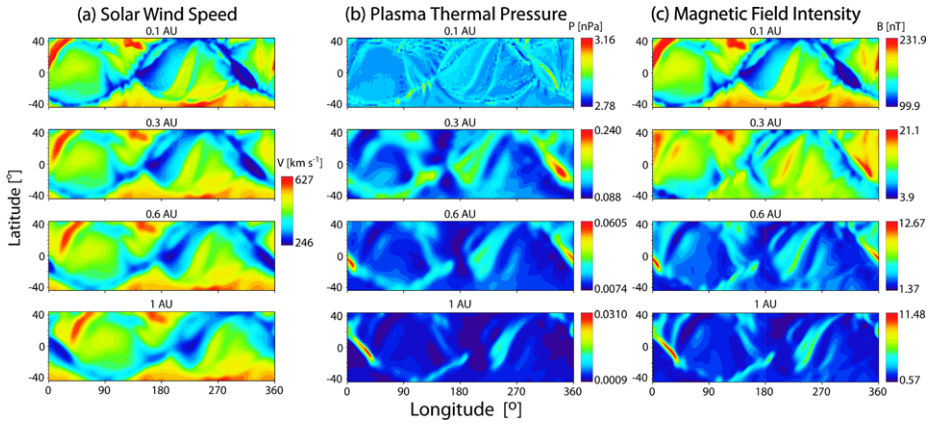

Figure 2 Color contours of (a) solar wind speed V, (b) plasma thermal pressure P, and (c) magnetic field intensity B from the old version (WSA v1.6 and Enlil v2.6) of the MWO-WSA-Enlil model at 0.1, 0.3, 0.6, and 1 AU for CR 2016. The color indication is given by the color scale. The longitudinal variation from 0° to 360° represents the temporal variation throughout one CR at the Earth. The results from the new version (WSA v2.2 and Enlil v2.7) of the MWO-WSA-Enlil model show similar radial variations.

line (approximated by the slow-wind belt) moved equator-ward by about 15° in longitudes 150° – 240° and became more twisted in longitudes 240° – 360° where the slow-wind region expanded too. Below we will compare the observations with the model results for each CR. As a summary, Figure 10 plots the simulation-to-observation offset or ratios for SIRs in CRs 2017 – 2018, and Figure 11 shows the simulation-to-observation ratios for baseline slow wind.

2.1. CR 2016

For CR 2016, we ran the MWO-WSA-Enlil model. Figure 1 provides the MWO synoptic photospheric magnetogram as input and the results from (a) old v1.6 and (b) new v2.2 of the WSA model at 21.5 R_s. The results from old and new WSA model are similar as expected because there are only subtle tuning differences between the two. There are several active regions in the low-latitude region, and this comparison indicates their effect for the solar wind. Figure 2 illustrates the radial evolution of solar wind speed V, plasma thermal pressure P, and magnetic field intensity B in steps from 0.1 to 1 AU using WSA v1.6 and Enlil v2.6. With the radial propagation, the region around the HCS is accelerated gradually; the difference of P between the HCS region and ambient solar wind increases slightly, while the field difference between the polar and low-latitude regions decreases significantly. The strong field changes from the polar region to the two patches along the tilted HCS, as expected for the compression at SIRs. The radial variations using the new WSA-Enlil model (not shown) are similar to the above.

In Figure 3(a), we compare the model results (red solid line for old version, red dashed line for new version) with ACE observations (black dots) at 1 AU during 2 – 29 May 2004. The solar wind speed V, proton number density N_p, and proton temperature T_p are obtained from the Solar Wind Electron, Proton and Alpha Monitor (SWEPAM) suite (McComas *et al.*, 1998), while the magnetic field B is from the Magnetic Field Experiment (Smith *et al.*, 1998). We use the sign of the azimuthal field to represent the observed field polarity, with positive for westward and inward field, because the sign of the radial field component has

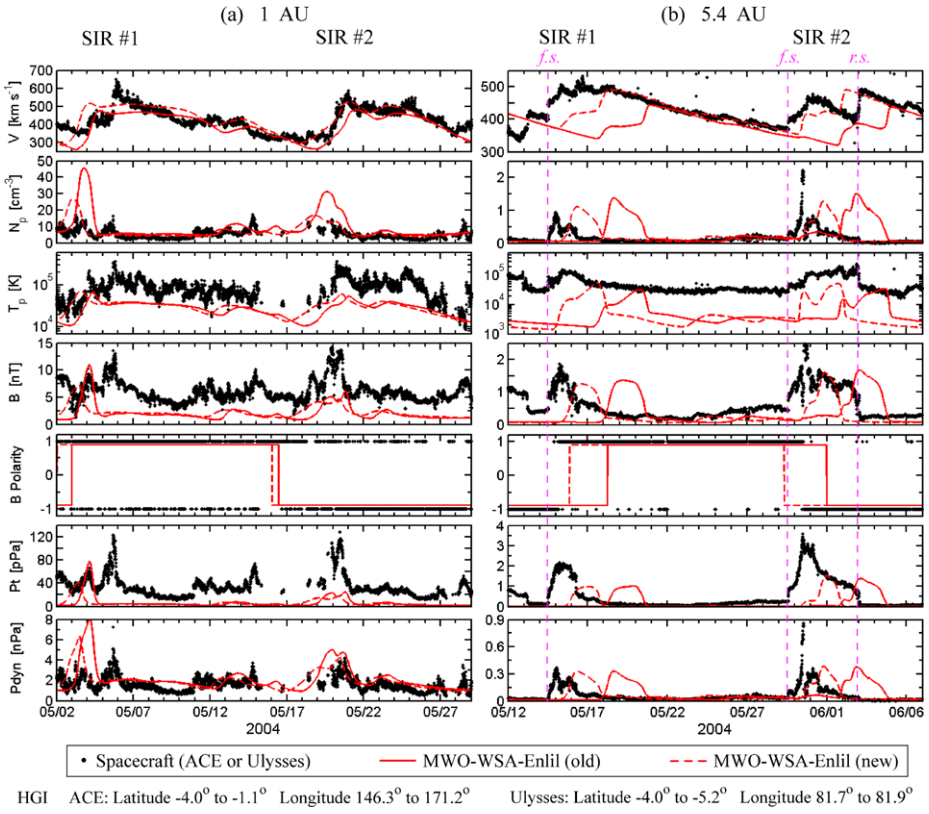

Figure 3 Comparison of Enlil model results with (a) ACE observations during 2 – 29 May 2004 and (b) *Ulysses* observations during 12 May – 7 June 2004. From top to bottom: solar wind speed V, proton number density N_p, proton temperature T_p, magnetic field intensity B, magnetic field polarity, total pressure P_t, and dynamic pressure P_{dyn}. The black dots are *in-situ* spacecraft observations; the solid and dashed red lines indicate the model results from old version and new version of MWO-WSA-Enlil model. The spacecraft positions in the heliographic inertial (HGI) coordinates are provided at the bottom. Because the orbital period of an object around the Sun at 5.4 AU is much longer than the sidereal rotation period of the Sun, we use the solar rotation period of 26 days to approximate the synodic rotation period and it is the time window of (b). The magenta dashed vertical lines mark the observed shocks, labeled f.s. for forward shock and r.s. for reverse shock.

more short-duration (1 – 2 days) back-and-forth switches and also because the field spiral is tight and the radial component is very small at 5.4 AU. In the simulation output, the field polarity is given as an individual parameter. The total pressure P_t and dynamic pressure P_{dyn} are combined parameters that approximately represent the interaction strength and the solar wind impact on the relatively static obstacles, such as planets.

We interpolate the observations to 8-min resolution to match the model output. The model reproduces the two SIRs and also the basic variations of the plasma and magnetic field parameters. The V, T_p, and B of SIR #1 increased by two steps on 4 and 5 May in ACE observations, but the second increases of these parameters are not captured by the model. For both SIRs at 1 AU, the old WSA-Enlil model overestimates N_p and P_{dyn}, and underestimates the other parameters. The new version predicts an earlier SIR occurrence and improves the

estimations of V, N_p, and T_p, but worsens the estimations of peak B and P_t. The modeled field polarity matches the observation, despite an approximate 2-day offset.

Figure 3(b) shows the comparison between the model results and *Ulysses* observations at 5.4 AU. The *in-situ* V, N_p, and T_p are obtained from the Solar Wind Observations Over the Poles of the Sun (SWOOPS) instrument (Bame *et al.*, 1992), and B is from the magnetometer (Balogh *et al.*, 1992). The new version of the model improves the SIR timing prediction and V estimation significantly. Both old and new versions underestimate T_p, for both the SIRs and ambient solar wind. The N_p and B increases at the two SIRs are reproduced well, except for the sudden jumps on 30 May. Combining these effects, the model underestimates the peak P_t by about a half and estimates the right peak P_{dyn}. The model captures all the shocks (magenta dashed lines) at 5.4 AU, except that the shock at the trailing edge of SIR #1 has not formed yet in observations. For SIR #2 at 5.4 AU, the time profiles of N_p, B, P_t, and P_{dyn} are asymmetric, with a rapid increase and gradual decline. Such features are roughly captured by the model, suggesting the model can describe the dynamics at this SIR. The model reproduces the sector boundaries with time delays of 2 – 3 days. In comparison with the Enlil v2.3a (not shown in this paper), versions 2.6 and 2.7 produce stronger N_p and P_{dyn} enhancements and capture the shocks better.

2.2. CR 2017

We ran three pairs of old and new models for CR 2017: the MWO-WSA-Enlil, NSO-WSA-Enlil, and NSO-MAS-Enlil models. The difference in the synoptic photospheric magnetograms from MWO and NSO (Figure 4) are not pronounced except that NSO has higher time resolution. However, the WSA coronal model derives remarkably different distributions of solar wind speed and coronal holes at 21.5 R_s from the two synoptic maps, as shown in Figure 4. The HCS approximated by the low-speed belt from the NSO-WSA model extends more pole-ward than the MWO-WSA model by about 7°. Such a variation of the HCS latitudinal span with the source magnetograph was also noted by other studies, *e.g.*, Neugebauer *et al.* (1998). In addition, the NSO-WSA model generates faster solar wind in the polar region (by over 50 km s^{-1} at some locations) and smaller slow-wind region than the MWO-WSA model. The results from the old and new versions of WSA model are similar except for some subtle changes at high latitudes.

Figure 5 compares V, N, T, P, and B from the three pairs of runs at 0.144 AU, the common innermost boundary of the three models. The old and new versions of models are arranged in parallel. The differences between the different models are apparent, so are the differences between the old and new versions of the same model. The NSO-WSA-Enlil model looks like an intermediate solution between the other two models, in terms of the differences of V, T, and B between the slow and fast wind. The NSO-WSA-Enlil model produces more structured slow-wind region than the MWO-WSA-Enlil model, probably because NSO has more sensitive instruments and better corrections to the polar field. Using the same synoptic magnetograph, the NSO-WSA-Enlil model shows more structure than the NSO-MAS-Enlil model, probably because MAS coronal model uses a simple adiabatic energy equation and a single polytropic index (Riley, Linker, and Mikić, 2001). The NSO-MAS-Enlil model produces more V and T discrepancies and a less P discrepancy for slow and fast wind regions than the other two models. The maximum B from the NSO-MAS-Enlil model is stronger than the other two models. These differences could be in part because that the MAS-Enlil model imposes some speed correction derived from an *ad hoc* description at 30 R_s (Riley, Linker, and Mikić, 2001). All the above differences directly affect the simulation output at 1 and 5.4 AU below.

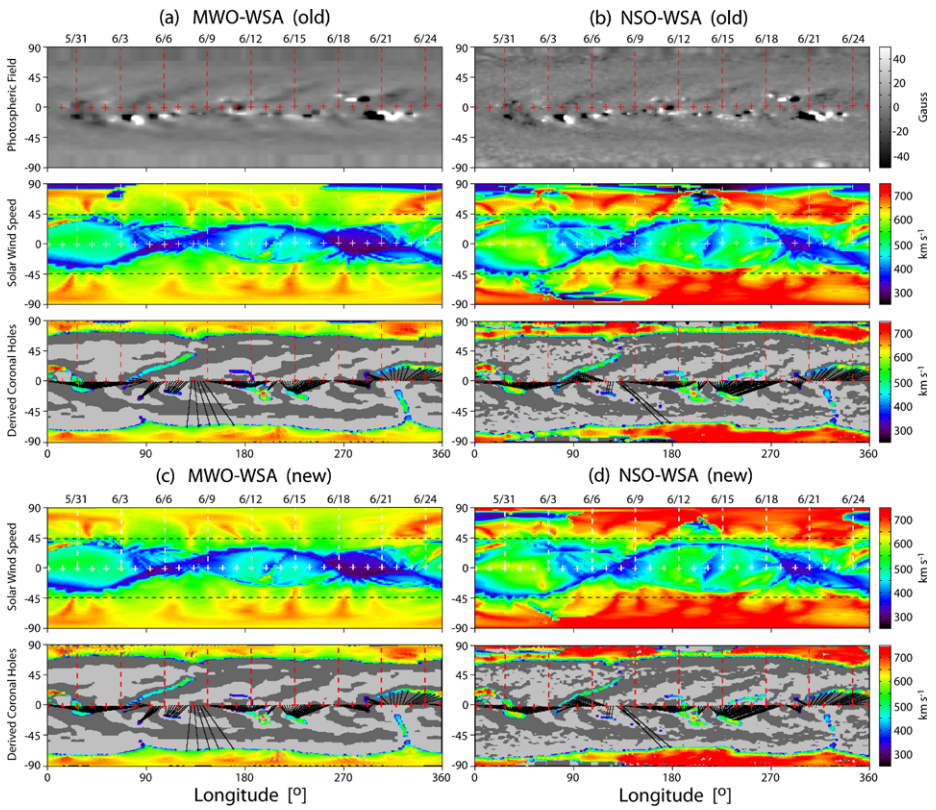

Figure 4 The coronal sources derived from the WSA coronal model based on (a, c) the MWO photospheric magnetograph and (b, d) the NSO photospheric magnetograph for CR 2017. Old version 1.6 of WSA is used for (a) and (b), while WSA v2.2 is used for (c) and (d). Captions of Figure 1 apply. The two dashed black lines in the panels of derived solar wind speed mark the latitudinal range covered in Figure 5.

Figure 6 displays the comparison between the observation and simulation results at 1 and 5.4 AU using seven parameters. The red, green, and blue lines indicate the MWO-WSA-Enlil, NSO-WSA-Enlil, and NSO-MAS-Enlil models, respectively; the solid and dashed lines denote old and new versions of models. Overall, the results of the three models differ from each other significantly and none of them matches the observations very well. One challenge is to identify the best way to improve their performance, given the number of influences each assumption of the model (and its boundaries) may have.

We highlight a few points of the comparison. Firstly, the simulated magnetic field polarities and sector boundaries roughly match with the observation at both 1 and 5.4 AU, with a few days offset similar to the interface offset of SIRs. Secondly, the new versions of models have improved the prediction of V and the resultant timing of SIRs and sector boundaries. The model (NSO-MAS-Enlil at 1 AU) estimating highest-speed fast wind does not predict the SIRs earlier than the other two models because it underestimates the duration of fast wind. The new versions of models have also improved the estimation of peak N_p, but the old and new versions both underestimate the background T_p even at 1 AU. Meanwhile, the simulated peak T_p is close to that observed for SIRs at 1 and 5.4 AU.

Thirdly, as the solar synoptic maps and coronal/heliospheric models have limited resolution, the leading and trailing edges of the two SIRs from these models almost mimic a

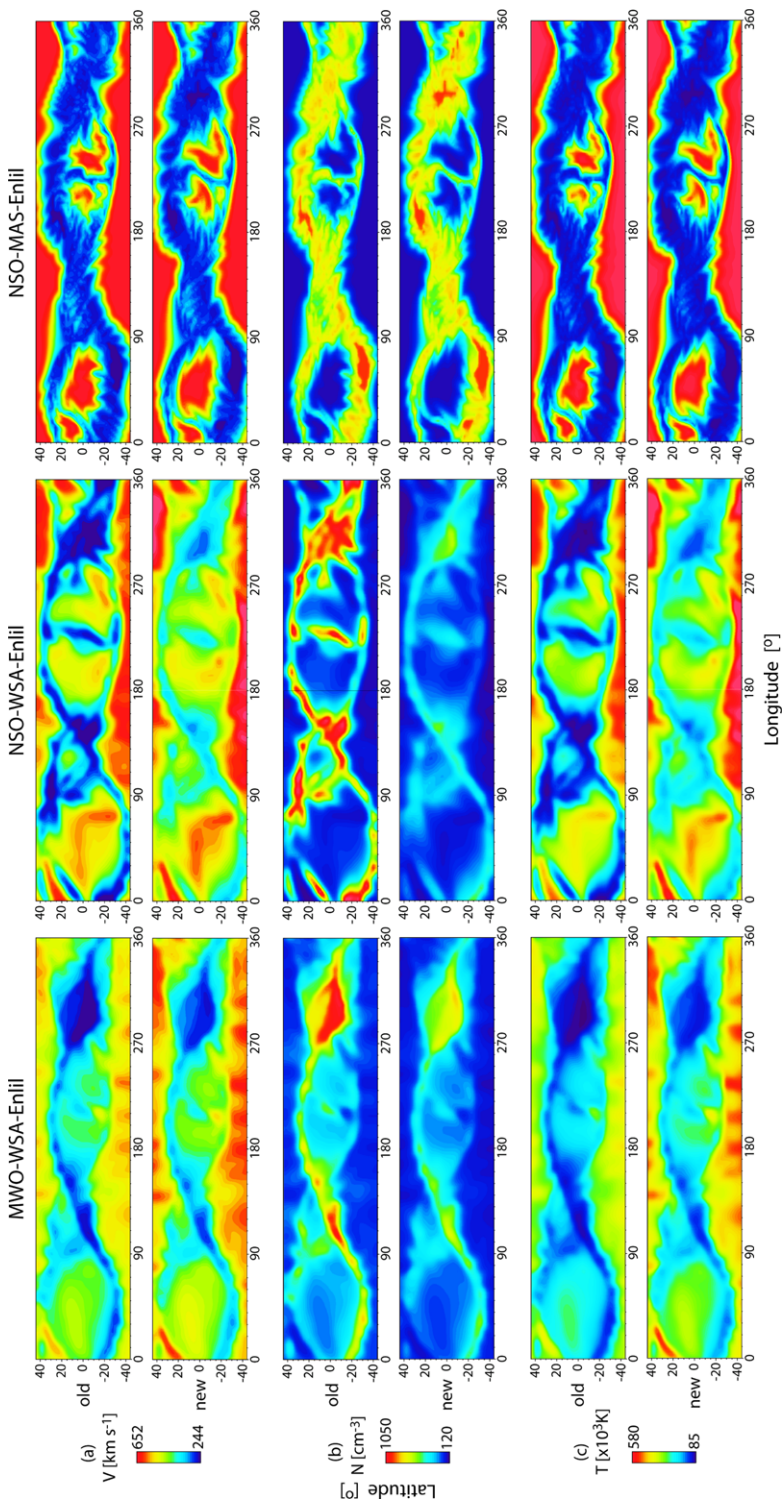

Figure 5 Inner boundary condition of the Enlil heliospheric model at 0.144 AU (31 R_S) in different runs for CR 2017: the MWO-WSA-Enlil, NSO-WSA-Enlil, and NSO–MAS-Enlil runs. The old and new versions of models are marked at the left. From top to bottom, the panels show (a) solar wind speed V, (b) particle number density N, (c) particle temperature T, (d) plasma thermal pressure P, (e) magnetic field intensity B. The color scale is the same for the six runs.

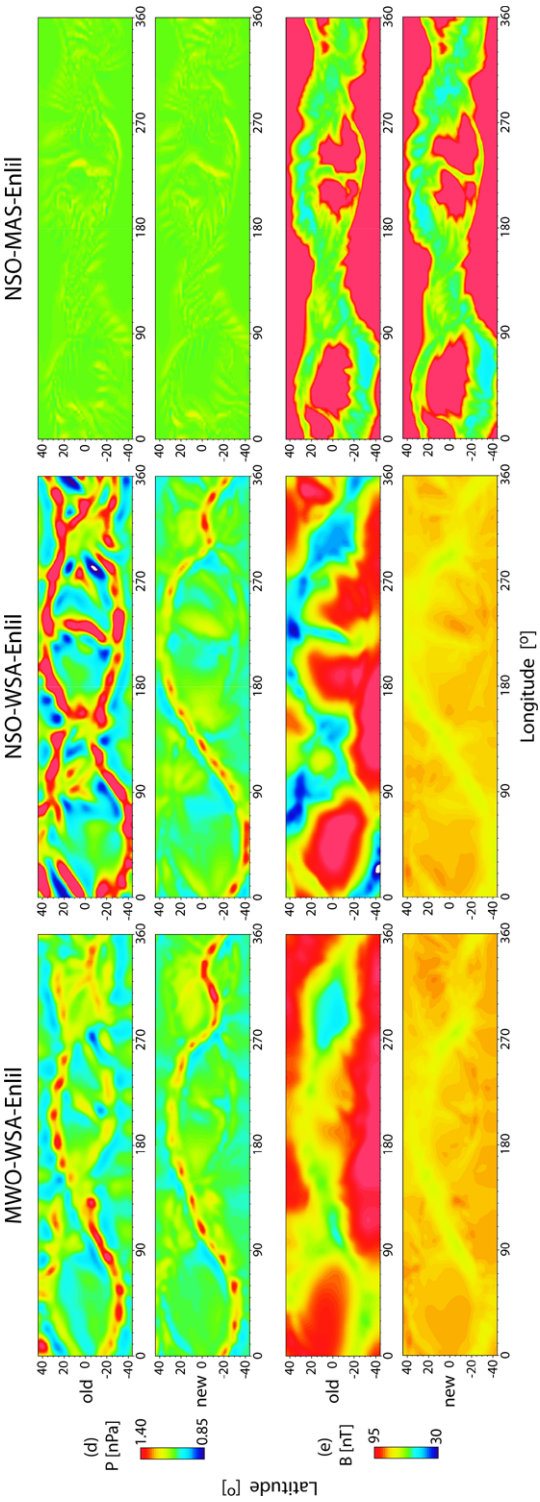

Figure 5 (*Continued*)

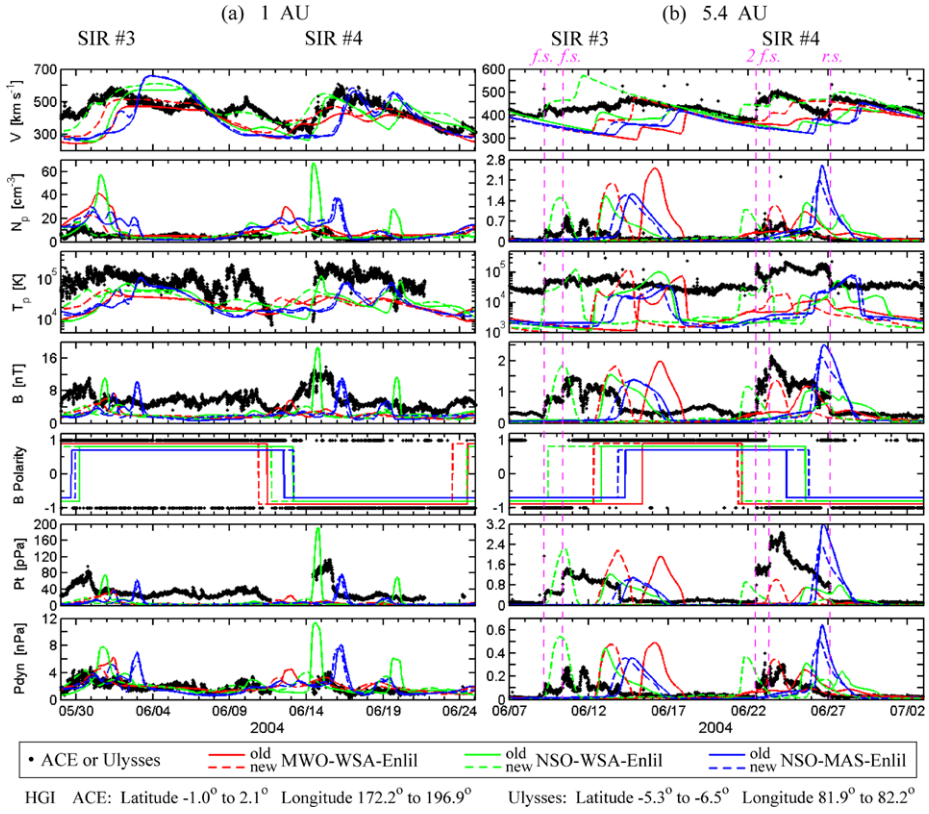

Figure 6 Comparison of the Enlil simulation results with (a) ACE observations at 1 AU during 29 May – 25 June 2004 and (b) *Ulysses* observations at 5.4 AU during 7 June – 3 July 2004. The black dots denote spacecraft observations; the solid (dashed) red, green and blue lines indicate the results from the old (new) version of MWO-WSA-Enlil, NSO-WSA-Enlil, and NSO-MAS-Enlil runs, respectively. The spacecraft locations are given at the bottom. From top to bottom are: V, N_p, T_p, B, magnetic field polarity, P_t, and P_{dyn}. The magenta dashed vertical lines mark the observed shocks.

pair of forward-reverse shocks but none of the models captures the observed double forward shocks leading SIRs #3 and #4 at 5.4 AU. Fourthly, from 1 to 5.4 AU, the order of SIR parameters among the six different runs shuffle. For example, the new NSO-WSA-Enlil model predicts the lowest B for SIR #3 at 1 AU, but the strongest B for the same SIR at 5.4 AU. The simulation-to-observation ratios of the SIR durations usually decrease with distance, as shown in Figure 10(b), indicating the compression force overcomes the expansion force.

2.3. CR 2018

As we did for CR2017, we ran three pairs of old and new models at CCMC for CR 2018: the MWO-WSA-Enlil, NSO-WSA-Enlil, and NSO-MAS-Enlil models. Similar to the comparison for CR 2017, in Figure 7, the NSO map displays more small-scale structures than the MWO map, and the WSA coronal model results at 21.5 R_s based on them are remarkably different. The derived HCS from the NSO-WSA model extends more pole-ward by $\approx 15°$ than from the MWO-WSA model, probably because the NSO-WSA model has stronger field from the low-latitude active regions and coronal holes. The high-latitude solar wind from the

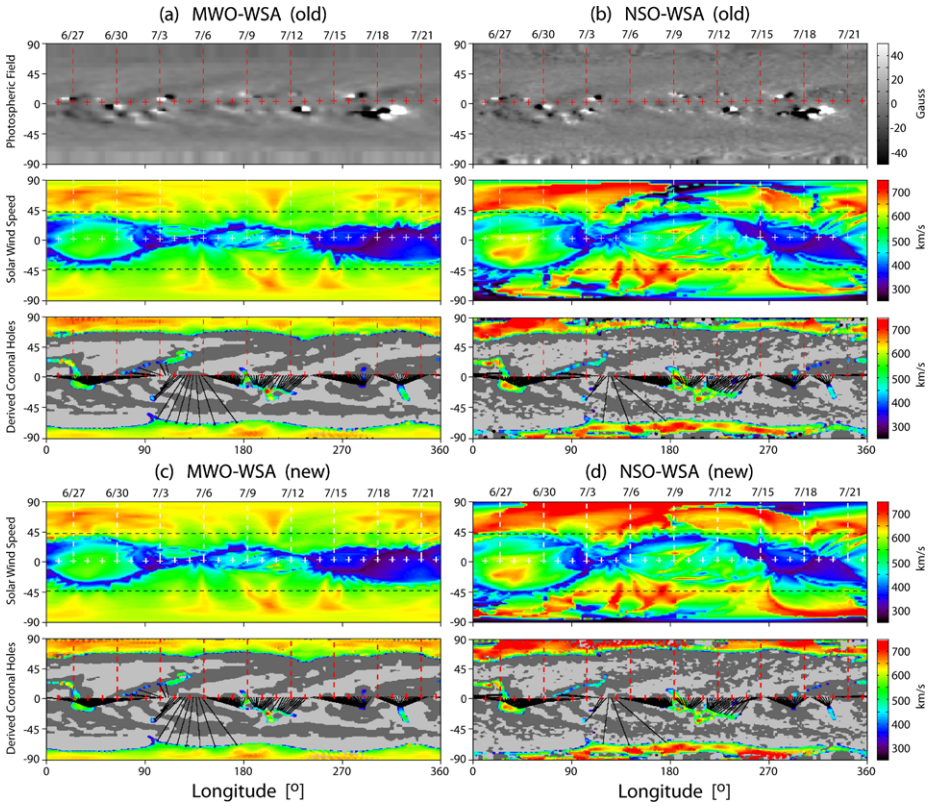

Figure 7 The coronal sources derived from the WSA coronal model based on (a, c) the MWO photospheric magnetograph and (b, d) the NSO photospheric magnetograph for CR 2018. Old v1.6 of WSA is used for (a) and (b), while WSA v2.2 is used for (c) and (d). Captions of Figure 1 apply. The two dashed black lines in the panels of derived solar wind speed mark the latitudinal range covered in Figure 8.

NSO-WSA model is faster than from the MWO-WSA model. The slow-wind speed distributions from the two models are different over longitudes 240° – 360°. The results from the old and new versions of WSA model are similar except some discrepancy in the derived speed distribution near the north polar region over longitudes 180° – 270°.

Figure 8 illustrates the color contours of V, N, T, P, and B from the three pairs of runs at 0.144 AU, the common innermost boundary of the heliospheric part. The HCSs from the NSO-WSA-Enlil and NSO-MAS-Enlil models extends more poleward than from the MWO-WSA-Enlil model. Similar to CR 2017, the slow-wind region from the NSO-MAS-Enlil model is wider than from the other two models. The inner boundary from the NSO-WSA-Enlil model is more structured than from the other two models, including two fast streams over longitudes 160° – 280°. The new NSO-WSA-Enlil model generates much weaker B than the MWO-WSA-Enlil model, causing weaker IMF to be predicted at 1 AU.

Figure 9 compares the observations and simulation results at 1 and 5.4 AU. ACE observed two more small SIRs after SIR #6, probably attributed to the highly twisted HCS and the low-latitude small coronal holes during the late period of the CR as shown in Figure 7. Among the three models, only the NSO-WSA-Enlil model produces a clear secondary V increase and a resultant weak SIR after SIR #6, consistent with the two fast streams over lon-

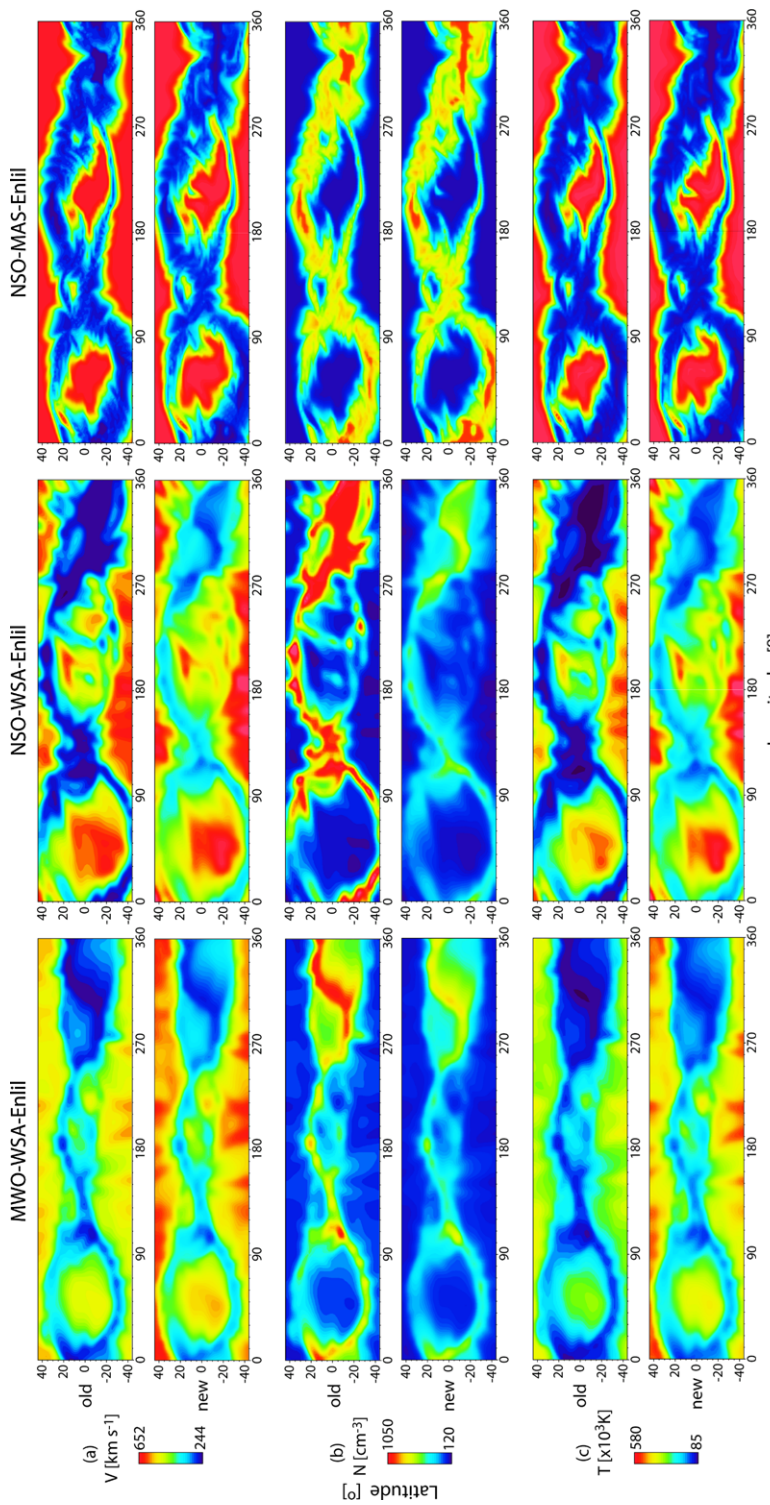

Figure 8 Inner boundary condition of the Enlil heliospheric model at 0.144 AU from the old and new versions of runs for CR 2018: the MWO-WSA-Enlil, NSO-WSA-Enlil, and NSO-MAS-Enlil runs. The captions of Figure 5 apply.

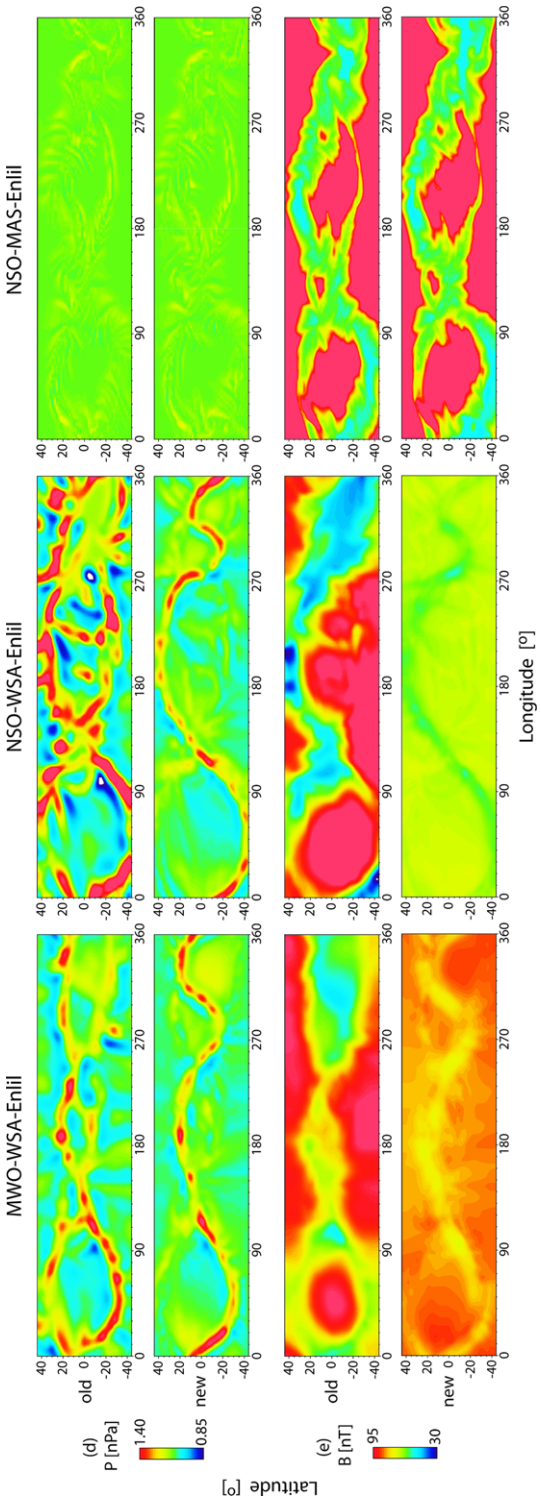

Figure 8 *(Continued)*

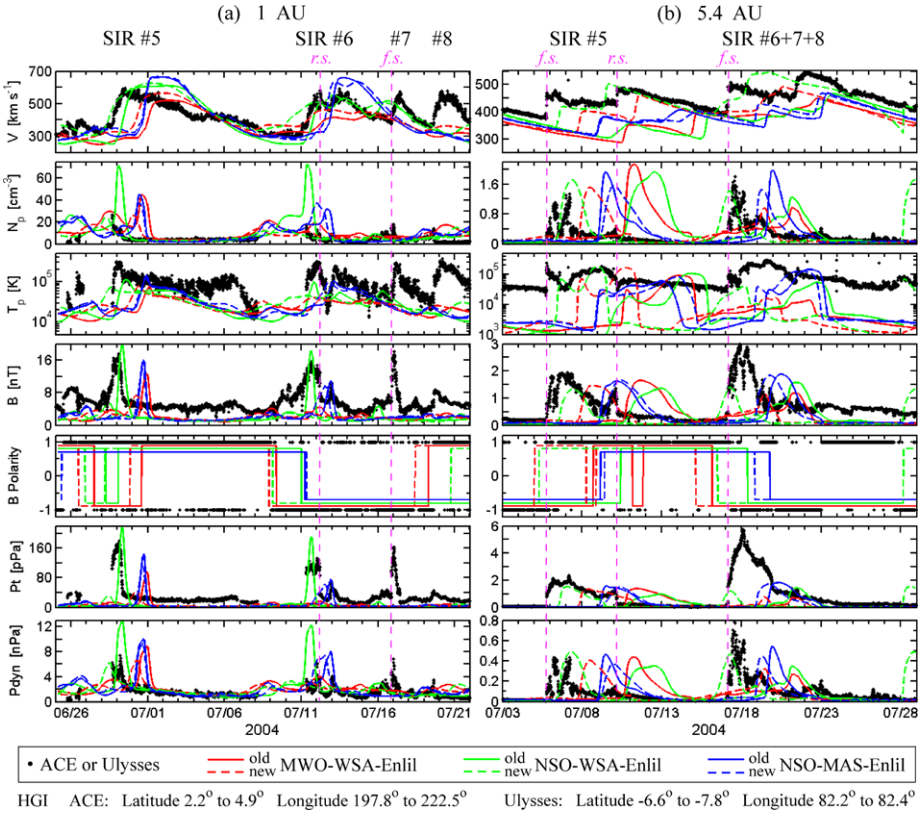

Figure 9 Comparison of the Enlil simulation results with (a) ACE observations at 1 AU during 25 June – 22 July 2004 and (b) *Ulysses* observations at 5.4 AU during 3 – 29 July 2004. The captions of Figure 6 apply.

gitudes 160° – 280° at the inner boundary generated by this model (Figure 8). We compare the model results only with SIR #6 in Figure 10, because it has a larger speed increase and a longer duration than the following two SIRs. ACE observed a reverse shock for SIR #6 and a forward shock for SIR #7, whose shock normal directions are $-0.90R - 0.43T - 0.06N$ and $0.40R + 0.77T - 0.49N$ in the RTN coordinates, respectively. As the two shocks roughly propagate against each other, these SIRs are expected to expand and merge into one SIR, as confirmed by the *Ulysses* observation during 17 – 24 July at 5.4 AU. The SIR #6 at 5.4 AU has a strong leading shock, a maximum B of 3 nT and a peak P_t of 6 pPa, higher than the typical values for SIRs at this distance, 2.2 nT and 3.5 pPa (Jian *et al.*, 2008b).

We highlight a few points about the comparison in Figure 9. Firstly, the simulated field polarities and sector boundaries roughly match the observation except for the short-term discrepancies at SIR #5 at 1 and 5.4 AU from MWO-WSA-Enlil and NSO-WSA-Enlil models. These discrepancies may be due to the emergence of opposite-polarity active region or small coronal hole at low latitudes near longitude 90° from the WSA coronal model (Figure 7). Secondly, the new versions of models have improved the estimation of V and the resultant SIR timing, especially at 5.4 AU. The new versions have also improved the estimation of N_p and P_{dyn}, but worsened the underestimation of the B and P_t enhancement, especially at 1 AU. All these models underestimate the background T_p at 5.4 AU by about an order of magnitude, similar to during CR 2017.

Thirdly, none of the models captures the shocks at 1 AU but they nearly all capture the forward-reverse shock pair of SIR #5 at 5.4 AU. At the leading edge of SIR #6, the simulated parameters from the MWO-WSA-Enlil model change too gradually to mimic the observed forward shock. The trailing edge of SIR #6 cannot be classified as a reverse shock in observations because the shock features in T_p and B are missing, but the pairs of NSO-MAS-Enlil model produce a reverse shock. This suggests the physical processes in the real solar wind are more complicated than can be described in the models. Some of the SIR-driven shocks are not well-developed at 5.4 AU and can be missed by a single-point observation. Fourthly, the order of SIR parameters among different runs can change from 1 to 5.4 AU as also shown in Figure 10. For example, the NSO-MAS-Enlil produces the fastest fast wind at 1 AU but the slowest fast wind at 5.4 AU. Fifthly, some of the models can reproduce the asymmetric temporal variations of SIR parameters, *e.g.*, the N_p and B variations of the two SIRs at 5.4 AU, indicating the models can capture some details of the interaction dynamics.

3. Discussion and Conclusions

We have chosen CRs 2016 – 2018 in 2004, when solar wind stream structures are observed by both ACE and *Ulysses* at 1 and 5.4 AU, respectively. The radial variations of the six SIRs agree with our statistical results on the 1-AU and 5.4-AU SIRs in Jian *et al.* (2006, 2008b). From 1 to 5.4 AU, the slow streams are accelerated while the fast streams are decelerated, and more shocks, usually forward-reverse shock pairs, are driven. In CR 2018, three small SIRs at 1 AU interacted and merged to a strong SIR at 5.4 AU. Such merging can partially explains why SIRs occur less often at a greater heliocentric distance (Jian *et al.*, 2008b).

We summarize the simulation-observation comparison of SIR features and baseline slow wind parameters for CRs 2017 – 2018 in Figures 10 and 11. There are four SIRs at each distance, and two versions of three models. For slow wind, we visually choose two quiet days before the first SIR in each CR at each distance, because the interval between the two SIRs is sometimes noisy especially in the model results. In Figures 10 and 11, the red, green, and blue indicate the MWO-WSA-Enlil, NSO-WSA-Enlil, NSO-MAS-Enlil models, respectively. The solid lines mark the averages for old and new versions of models. The dashed lines denote the averages at 1 and 5.4 AU. The simulation results differ from the observations widely as indicated by the scales of vertical axes. In the following, we will evaluate first the SIR simulation and then the solar wind simulation. For each parameter, we will consider *i*) three different models, *ii*) two different versions, *iii*) 1 AU *vs.* 5.4 AU.

First of all, the Enlil model can generally reproduce the field polarities and sector boundaries, and roughly capture the occurrence and features of SIRs, but it cannot precisely predict the timing of the SIRs and sector boundaries. From Figure 10, the new versions of models have significantly improved the timing prediction. The best performer is the new MWO-WSA-Enlil model (half a day later than observation on average), then the new NSO-MAS-Enlil model (one day earlier on average). The timing prediction is later at 5.4 AU than at 1 AU for all the models. The new versions do not change the prediction of SIR duration much. The models generally overestimate the duration at 1 AU and underestimate the duration at 5.4 AU, implying they can simulate enough compression at SIRs from 1 to 5.4 AU but not sufficiently within 1 AU.

The new versions of models have improved the prediction of the fastest V. The best performer is the new NSO-WSA-Enlil model, then the NSO-MAS-Enlil (new and old versions have similar results). There is no clear radial variation trend for the simulation-to-observation ratio of fastest V. The new versions have improved the estimation of the N_p

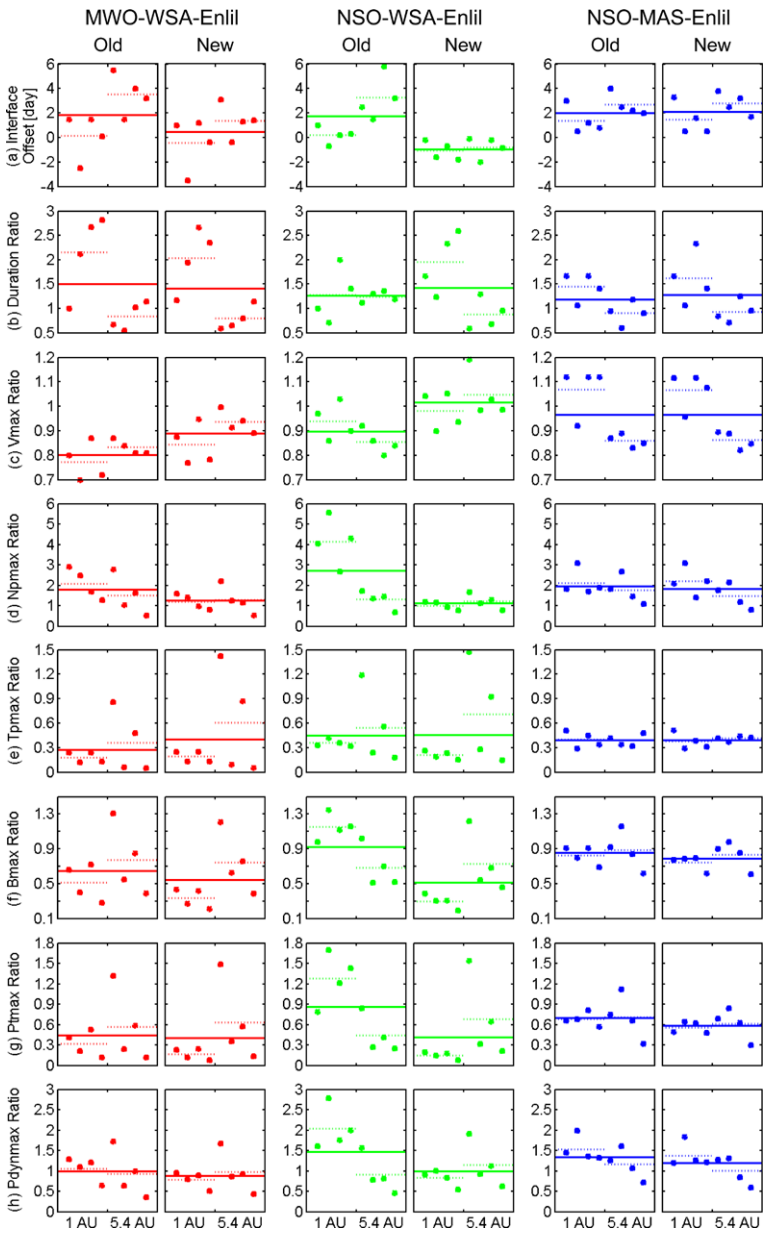

Figure 10 The comparison of simulated parameters with observations for eight SIRs during CRs 2017 – 2018. Red, green, and blue dots or lines denote the results from the MWO-WSA-Enlil, NSO-WSA-Enlil, and NSO-MAS-Enlil runs, respectively. In each box, the first four points are results at 1 AU and the last four points are results at 5.4 AU. The dashed lines indicate the corresponding averages of SIRs at 1 and 5.4 AU, and the solid line marks the average of the eight points in each box. The results from old and new versions of models are arranged in parallel for comparison. From top to bottom are: (a) stream interface offset (– for simulated earlier than observed), (b) duration ratio, (c) maximum V ratio, (d) ratio of maximum N_{p}, (e) maximum T_{p} ratio, (f) ratio of maximum B, (g) ratio of maximum P_{t}, (h) ratio of maximum P_{dyn}. The ratios are all of the simulated parameters to the observed ones.

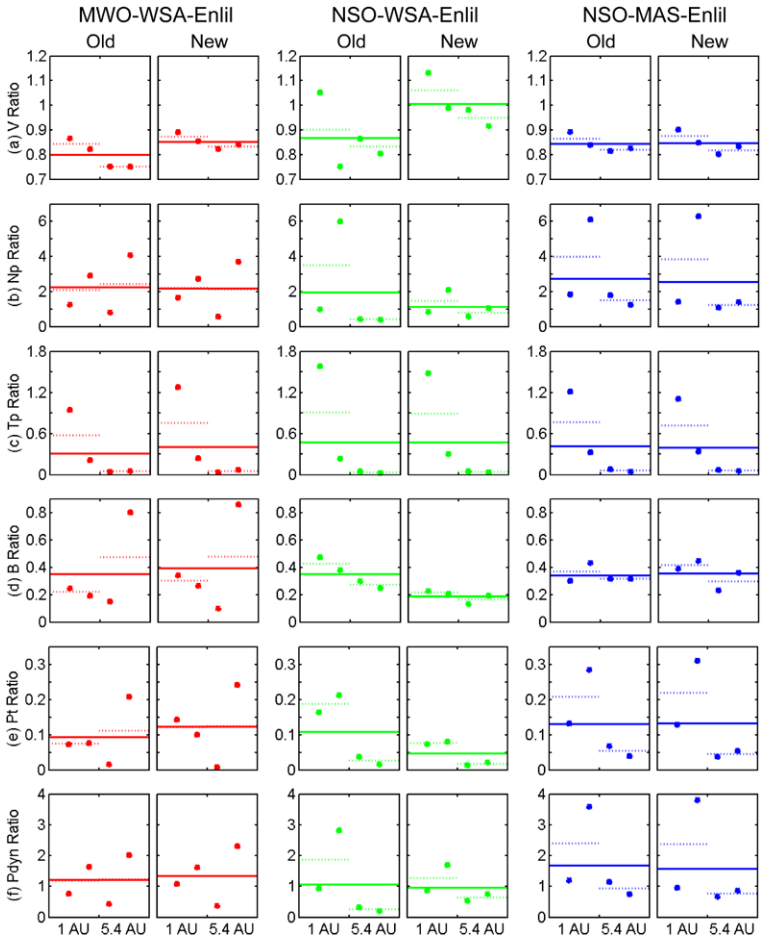

Figure 11 The comparison of simulated parameters with observations for slow wind during CRs 2017 – 2018. Red, green, and blue dots or lines indicate the results from MWO-WSA-Enlil, NSO-WSA-Enlil, NSO-MAS-Enlil models. In each box, the first two points denote the results at 1 AU, while the last two points for 5.4 AU. The dashed lines mark the averages at 1 and 5.4 AU. The solid line in each box denotes the average of four points. From top to bottom, the simulation-to-observation ratios are plotted: (a) V ratio, (b) N_{p} ratio, (c) T_{p} ratio, (d) B ratio, (e) P_{t} ratio, (f) P_{dyn} ratio.

compression at SIRs, although still overestimate it. As a combination of V and N_{p}, the prediction of maximum P_{dyn} at SIRs has been improved in the new models. There is no clear radial variation of the prediction for the N_{p} compression and P_{dyn} increase.

All the models underestimate the highest T_{p} at SIRs. The new versions have improved the prediction a little, but their average predictions are still less than half of the observation. The prediction of the highest T_{p} is better at 5.4 AU than at 1 AU. All of the models underestimate the field compression, and the new versions worsen the prediction. The best performer is the old NSO-WSA-Enlil model, mainly because the free parameters of the new version have not been pre-calibrated on as many CRs as the old version and the setting of the new scaling factor is not mature. The prediction of the maximum field is better at 5.4 AU than at 1 AU for these runs except the old NSO-WSA-Enlil model. As a hybrid parameter, all the

models underestimate P_t and the new versions worsen the estimation because of the field contribution. The best performer is again the old NSO-WSA-Enlil model. The performance of different models can change the order from 1 to 5.4 AU. When the temporal profiles of parameters are asymmetric, the models cannot necessarily reproduce the locations of the peak values with respect to the whole event. Moreover, the MWO-WSA-Enlil and NSO-MAS-Enlil models cannot capture the transient and small SIRs #7 and #8 at 1 AU which have clear SIR signatures in the observations.

About the baseline slow wind (Figure 11), the models generally underestimate V and overestimate N_p. The new versions of the models improve the prediction of these two parameters, but worsen the underestimation of B and P_t. Such variations from old to new versions are similar to the prediction of SIR parameters. P_t even in the best performer (NSO-MAS-Enlil) is weaker than the observed by more than 85% at 1 and 5.4 AU. All the models greatly underestimate T_p up to an order of magnitude at 5.4 AU, suggesting the models need to add more solar wind heating. Although T_p is not critical to solar wind evolution, it is a key parameter to determine the sonic speed and magnetosonic speed of solar wind and thus related to the shock parameter and solar energetic particle (SEP) propagation. There are multiple heating mechanisms proposed, such as, energy transfer from the damping of the ion cyclotron waves to the solar wind ions (*e.g.*, Cranmer, 2000, 2004; Isenberg, 2001; Russell *et al.*, 2008; Jian *et al.*, 2009, 2010; and references therein), ion heating at current sheets generated by strong and non-propagating MHD turbulence (*e.g.*, Matthaeus *et al.*, 1999; Dmitruk *et al.*, 2002; Dmitruk, Matthaeus, and Seenu, 2004), and plasma heating through the propagation of shock waves from lower altitudes into the corona (*e.g.*, Berdichevsky *et al.*, 1997; Lee and Wu, 2000).

The discrepancies between the simulations and observations can be attributed to several factors. First, the resolution of solar magnetic field observations is too low to pick up regions of open field lines that are spatially small or transient (Neugebauer *et al.*, 1998). The synoptic maps are never true snapshots of the photospheric field because they are constructed from a 27-day sequence of (usually) daily full-disk magnetograms. Field evolution can be occurring at poorly observed or invisible parts of the Sun in the meantime, which is not accounted for in the maps used in these models, especially when active regions are still present on the Sun, because they tend to evolve faster than the solar rotation. In fact, during CRs 2016 – 2018, there were a considerable number of active regions on the Sun which can be quite non-potential. Their presence brings challenges to correctly model the coronal hole geometry, even for the MAS model which uses MHD (Riley *et al.*, 2006).

Second, although the step time of the Enlil output is about 8 min, the effective time resolution is limited by the spatial resolutions of the solar magnetogram and coronal models (about 2.5° in longitude or 4.5 h) and also by the Enlil computational grids. We chose the $1280 \times 45 \times 180$ grid for the above runs, which is the highest available at CCMC. The corresponding model resolution is only 0.0078 AU ($\approx$40 min assuming the solar wind speed of 500 km s^{-1}) in radial distance, 2° in longitude and latitude for the 10-AU heliosphere. Converting the 360°-longitude range to one CR, the time resolution is about 3.6 h. Models with such low resolution cannot capture small-scale structures in the solar wind, in particular, shocks and fast-slow stream boundaries. For example, none of the models captures the double forward shocks during CR 2017. To resolve variations within such as 10-min duration, the grids in the radial and longitudinal directions need to be $\approx$5120 and 4000 for a 10-AU heliosphere, or 1024 and 800 for a 2-AU heliosphere. The current finest grid for 2-AU is $1024 \times 120 \times 360$ at CCMC, so the desirable high resolution grid is probably feasible for some test runs. This discussion also raises the issue of the outer boundary. *Ulysses* provided an important and unique solar wind data set with its aphelion pass at 5.4 AU, its

high latitude perspective, and its long-term observations. Adding the option of 5.5 or 6 AU for the Enlil outer boundary at CCMC can add the science return from *Ulysses* and benefit the investigation of the space environment for Jupiter. Such interest will rise as the Juno spacecraft approaches Jupiter orbit.

Because all observatories have their own special ways of constructing and correcting the synoptic maps (*e.g.*, Neugebauer *et al.*, 1998; Arge and Pizzo, 2000; and references therein), the WSA and MAS models using synoptic maps from different sources can generate results with significant differences. For CRs 2017 and 2018, although the MWO and NSO solar field maps look similar, the NSO-WSA model gives a more pole-ward HCS, faster and hotter solar wind from the polar region at 21.5 R_s than the MWO-WSA model. At 1 AU, the NSO-WSA-Enlil model produces faster and hotter fast wind as well as earlier SIR occurrence than the MWO-WSA-Enlil model. The difference due to different coronal models (WSA *vs.* MAS) is as striking as the one caused by different synoptic maps. Using the same NSO synoptic map, at 0.144 AU, the NSO-MAS-Enlil model has more pronounced differences between fast and slow wind in terms of V, T, and B than the NSO-WSA-Enlil model, partially due to the *ad hoc* correction of the wind speed at 30 R_s in the MAS model. Although the NSO-MAS-Enlil model produces faster-speed fast wind than the NSO-WSA-Enlil model, as also noted by Lee *et al.* (2009), because it estimates a shorter duration for the fast wind, it predicts later SIR occurrence.

It would also be helpful to have access to inter-calibrated magnetograms from multiple sources, which have a higher level of confidence in the absolute field strength and also validated corrections to the observationally challenging polar fields (Owens *et al.*, 2005; Lee *et al.*, 2009). Before such map becomes available, our comparison suggests that when we do not know which solar synoptic map or which coronal model is more reliable, it is instructive to run the heliospheric model using multiple solar magnetograms and multiple coronal models. The CCMC has plans to take the magnetograms from the Michelson Doppler Imager (Scherrer *et al.*, 1995) of the Solar and Heliospheric Observatory (SOHO), and from the Helioseismic and Magnetic Imager of the Solar Dynamics Observatory (SDO) which provides magnetographs with a high spatial resolution of 1 arcsec and a time cadence of about 1 min.

Because we do not have *in-situ* observations within 30 R_s, it is difficult to evaluate the different coronal models quantitatively. At present, we can use the heliospheric model results evolved from the coronal models, or the images in extreme ultraviolet (EUV) and soft X-rays to indirectly assess the coronal models. The CCMC can in principle provide simulated coronal hole maps and/or polarized brightness maps as coronal model output, as has been provided by the Predictive Science, Inc. These maps can be compared with coronal observations to provide at least a qualitative validation. Future missions, such as the Solar Orbiter (Marsch *et al.*, 2005) or Solar Probe Plus (McComas *et al.*, 2005), will make critical observations in the outer corona and innermost heliosphere that will also greatly benefit coronal and heliospheric models.

The Enlil runs at the CCMC are conducted promptly after submission, usually taking shorter than one week, and the interface to the models provides a useful and convenient tool for analyzing and predicting the solar wind parameters in the inner heliosphere. We have demonstrated significant changes from WSA v1.6 to v2.2 and from Enlil v2.6 to v2.7. As the model codes are constantly updated by their developers, it is important to run and validate the new versions in systematic ways to test the effects of the changes made. In addition, the CCMC has increased the number of coronal and heliospheric models that it serves, and now includes, for example, the Space Weather Modeling Framework from the University of Michigan. More model combinations and more synoptic map sources will soon be offered at

the CCMC. Limited by the latitudinal alignment of ACE and *Ulysses*, we only investigated three CRs here. To obtain more convincing statistics on the model performance, we will continue to study more CRs under different solar wind conditions. We will also include the comparisons with multi-spacecraft observations including those from the *Solar Terrestrial Relations Observatory* (STEREO) twin spacecraft (Kaiser *et al.*, 2008) and ACE or *Wind* at the Sun–Earth Lagrange point L1.

Acknowledgements This research is supported by the NSF SHINE program through Award AGS-1062105 and NASA STEREO program through Grant NAS5-03131 administered by UC Berkeley. We appreciate CCMC staff for running the coronal and heliospheric models. We thank all the PIs of ACE and *Ulysses* for making the data available. We acknowledge the MWO and NSO staff for providing the photospheric magnetic data. We thank Nick Arge for providing the WSA coronal model at the CCMC. Work at Los Alamos was performed under the auspices of the U.S. Department of Energy, with financial support from the NASA ACE and STEREO programs. CISM (Center for Integrated Space Weather Modeling), supported by the NSF Science and Technology Center Program through Fund ATM-0120950 to Boston University, has contributed to the development of several of the models applied in this report.

References

Altschuler, M.A., Newkirk, G. Jr.: 1969, Magnetic fields and the structure of the solar corona. *Solar Phys.* **9**, 131.

Arge, C.N., Pizzo, V.J.: 2000, Improvement in the prediction of solar wind conditions using real-time solar magnetic field updates. *J. Geophys. Res.* **105**, 10465.

Arge, C.N., Odstrcil, D., Pizzo, V.J., Mayer, L.: 2002, Improved method for specifying solar wind speed near the Sun. In: Velli, M., Bruno, R. (eds.) *Solar Wind Ten*, *AIP Conf. Proc.* **679**, 190.

Arge, C.N., Luhmann, J.G., Odstrcil, D., Schrijver, C.J., Li, Y.: 2004, Stream structure and coronal sources of the solar wind during the May 12th, 1997 CME. *J. Atmos. Solar-Terr. Phys.* **66**, 1295.

Balogh, A., Beek, T.J., Forsyth, R.J., Hedgecock, P.C., Marquedant, R.J., Smith, E.J., Southwood, D.J., Tsurutani, B.T.: 1992, The magnetic field investigation on the *Ulysses* mission – Instrumentation and preliminary scientific results. *Astron. Astrophys. Suppl.* **92**, 221.

Bame, S.J., McComas, D.J., Barraclough, B.L., Phillips, J.L., Sofaly, K.J., Chavez, J.C., Goldstein, B.E., Sakurai, R.K.: 1992, The *Ulysses* solar wind plasma experiment. *Astron. Astrophys. Suppl.* **92**, 237.

Berdichevsky, D., Geiss, J., Gloeckler, G., Mall, U.: 1997, Excess heating of He^{2+} and O^{6+} relative to H^{+} downstream of interplanetary shocks. *J. Geophys. Res.* **102**, 2623.

Cranmer, S.R.: 2000, Ion cyclotron wave dissipation in the solar corona: The summed effect of more than 2000 ion species. *Astrophys. J.* **532**, 1197.

Cranmer, S.R.: 2004, Coronal heating versus solar wind acceleration. In: Walsh, R.W., Ireland, J., Danesy, D., Fleck, B. (eds.) *Proc. SOHO-15 Workshop – Coronal Heating* **SP-575**, ESA, Noordwijk, 154.

Dmitruk, P., Matthaeus, W.H., Seenu, N.: 2004, Test particle energization by current sheets and nonuniform fields in magnetohydrodynamic turbulence. *Astrophys. J.* **617**, 667.

Dmitruk, P., Matthaeus, W.H., Milano, L.J., Oughton, S., Zank, G.P., Mullan, D.J.: 2002, Coronal heating distribution due to low-frequency, wave-driven turbulence. *Astrophys. J.* **575**, 571.

Du, D., Wang, C., Hu, Q.: 2007, Propagation and evolution of a magnetic cloud from ACE to *Ulysses*. *J. Geophys. Res.* **112**, A09101.

Harvey, J.W., Hill, F., Hubbard, R.P., Kennedy, J.R., Leibacher, J.W., Pintar, J.A., *et al.*: 1996, The Global Oscillation Network Group (GONG) project. *Science* **272**, 1284.

Isenberg, P.A.: 2001, Heating of coronal holes and generation of the solar wind by ion-cyclotron resonance. *Space Sci. Rev.* **95**, 119.

Jian, L.K., Russell, C.T., Luhmann, J.G.: 2011, Comparing solar minimum 23/24 with historical solar wind records at 1 AU. *Solar Phys.* doi:10.1007/s11207-011-9737-2.

Jian, L., Russell, C.T., Luhmann, J.G., Skoug, R.M.: 2006, Properties of stream interactions at one AU during 1995 – 2004. *Solar Phys.* **239**, 337.

Jian, L.K., Russell, C.T., Luhmann, J.G., Skoug, R.M., Steinberg, J.T.: 2008a, Stream interactions and interplanetary coronal mass ejections at 0.72 AU. *Solar Phys.* **249**, 85.

Jian, L.K., Russell, C.T., Luhmann, J.G., Skoug, R.M., Steinberg, J.T.: 2008b, Stream interactions and interplanetary coronal mass ejections at 5.3 AU near the solar ecliptic plane. *Solar Phys.* **250**, 375.

Jian, L.K., Russell, C.T., Luhmann, J.G., Skoug, R.M.: 2008c, Evolution of solar wind structures from 0.72 to 1 AU. *Adv. Space Res.* **41**, 259.

Jian, L.K., Russell, C.T., Strangeway, R.J., Leisner, J.S., Galvin, A.B.: 2009, Ion cyclotron waves in the solar wind observed by STEREO near 1 AU. *Astrophys. J. Lett.* **701**, 105.

Jian, L.K., Russell, C.T., Luhmann, J.G., Anderson, B.J., Boardsen, S.A., Strangeway, R.J., Cowee, M.M., Wennmacher, A.: 2010, Observations of ion cyclotron waves in the solar wind near 0.3 AU. *J. Geophys. Res.* **115**, A12115.

Kaiser, M.L., Kucera, T.A., Davila, J.M., St. Cyr, O.C., Guhathakurta, M., Christian, E.: 2008, The STEREO mission: An introduction. *Space Sci. Rev.* **136**, 5.

Lee, C.O., Luhmann, J.G., Odstrcil, D., MacNeice, P.J., de Pater, I., Riley, P., Arge, C.N.: 2009, The solar wind at 1 AU during the declining phase of solar cycle 23: Comparison of 3D numerical model results with observations. *Solar Phys.* **254**, 155.

Lee, L., Wu, B.: 2000, Heating and acceleration of protons and minor ions by fast shocks in the solar corona. *Astrophys. J.* **535**, 1014.

Leibacher, J.W.: 1999, The global oscillation network group (GONG) project. *Adv. Space Res.* **24**, 173.

MacNeice, P.: 2009, Validation of community models: 2. Development of a baseline using the Wang–Sheeley–Arge model. *Space Weather* **7**, S12002.

Marsch, E., Marsden, R., Harrison, R., Wimmer-Schweingruber, R., Fleck, B.: 2005, Solar Orbiter – Mission profile, main goals and present status. *Adv. Space Res.* **36**, 1360.

Matthaeus, W.H., Zank, G.P., Oughton, S., Mullan, D.J., Dmitruk, P.: 1999, Coronal heating by magnetohydrodynamic turbulence driven by reflected low-frequency waves. *Astrophys. J. Lett.* **523**, 93.

McComas, D.J., Bame, S.J., Barker, P., Feldman, W.C., Phillips, J.L., Riley, P., Griffee, J.W.: 1998, Solar wind electron proton alpha monitor (SWEPAM) for the Advanced Composition Explorer. *Space Sci. Rev.* **86**, 563.

McComas, D.J., Velli, M., Lewis, W.S., Acton, L.W., Balat-Pichelin, M., Bothmer, V., *et al.*: 2005, Probe Solar: Humanity's first visit to a star. In: Fleck, B., Zurbuchen, T.H., Lacoste, H. (eds.) *Proc. Solar Wind 11 / SOHO 16 Workshop – Connecting Sun and Heliosphere* **SP-592**, ESA, Noordwijk, 279.

Neugebauer, M., Forsyth, R.J., Galvin, A.B., Harvey, K.L., Hoeksema, J.T., Lazarus, A.J., *et al.*: 1998, Spatial structure of the solar wind and comparisons with solar data and models. *J. Geophys. Res.* **103**, 14587.

Odstrcil, D.: 2003, Modeling 3D solar wind structure. *Adv. Space Res.* **32**, 497.

Odstrcil, D., Linker, J.A., Lionello, R., Mikić, Z., Riley, P., Pizzo, V.J., Luhmann, J.G.: 2002, Merging of coronal and heliospheric numerical two-dimensional MHD models. *J. Geophys. Res.* **107**, 1493.

Owens, M.J., Arge, C.N., Spence, H.E., Pembroke, A.: 2005, An event-based approach to validating solar wind speed predictions: High-speed enhancements in the Wang–Sheeley–Arge model. *J. Geophys. Res.* **110**, A12105.

Owens, M.J., Spence, H.E., McGregor, S., Hughes, W.J., Quinn, J.M., Arge, C.N., Riley, P., Linker, J., Odstrcil, D.: 2008, Metrics for solar wind prediction models: Comparison of empirical, hybrid, and physics-based schemes with 8 years of L1 observations. *Space Weather* **6**, S08001.

Parker, E.N.: 1963, *Interplanetary Dynamical Processes*, Wiley-Interscience, New York.

Pierce, A.K.: 1969, The solar program of the Kitt Peak National Observatory. *Solar Phys.* **6**, 498.

Richardson, I.G., Cliver, E.W., Cane, H.V.: 2000, Sources of geomagnetic activity over the solar cycle: Relative importance of coronal mass ejections, high-speed streams, and slow solar wind. *J. Geophys. Res.* **105**, 18203.

Riley, P., Linker, J.A., Mikić, Z.: 2001, An empirically-driven global MHD model of the solar corona and inner heliosphere. *J. Geophys. Res.* **106**, 15889.

Riley, P., Linker, J.A., Mikić, Z., Lionello, R.: 2001, MHD modeling of the solar corona and inner heliosphere: Comparison with observations. In: Song, P., Singer, H.J., Siscoe, G.L. (eds.) *Space Weather*, *AGU Geophys. Monogr.* **125**, 159.

Riley, P., Linker, J.A., Mikić, Z., Lionello, R., Ledvina, S.A., Luhmann, J.G.: 2006, A comparison between global solar magnetohydrodynamic and potential field source surface model results. *Astrophys. J.* **653**, 1510.

Russell, C.T., Jian, L.K., Luhmann, J.G., Zhang, T.L., Neubauer, F.M., Skoug, R.M., Blanco-Cano, X., Omidi, N., Cowee, M.M.: 2008, Mirror mode waves: Messengers from the coronal heating region. *Geophys. Res. Lett.* **35**, L15101.

Schatten, K.H.: 1971, Current sheet magnetic model for the solar corona. *Cosm. Electrodyn.* **2**, 232.

Schatten, K.H., Wilcox, J.M., Ness, N.F.: 1969, A model of interplanetary and coronal magnetic fields. *Solar Phys.* **6**, 442.

Scherrer, P.H., Bogart, R.S., Bush, R.I., Hoeksema, J.T., Kosovichev, A.G., Schou, J., *et al.*: 1995, The solar oscillation investigation – Michelson Doppler Imager. *Solar Phys.* **162**, 129.

Skoug, R.M., Feldman, W.C., Gosling, J.T., McComas, D.J., Reisenfeld, D.B., Smith, C.W., Lepping, R.P., Balogh, A.: 2000, Radial variation of solar wind electrons inside a magnetic cloud observed at 1 and 5 AU. *J. Geophys. Res.* **105**, 27269.

Smith, E.J., Wolfe, J.H.: 1976, Observations of interaction regions and corotating shocks between one and five AU: Pioneers 10 and 11. *J. Geophys. Res.* **3**, 137.

Smith, C.W., L'Heureux, J., Ness, N.F., Acuña, M.H., Burlaga, L.F., Scheifele, J.: 1998, The ACE magnetic field experiment. *Space Sci. Rev.* **86**, 613.

Toth, G., Odstrcil, D.: 1996, Comparison of some flux corrected transport and total variation diminishing numerical schemes for hydrodynamic and magnetohydrodynamic problems. *J. Comput. Phys.* **128**, 82.

Ulrich, R.K., Evans, S., Boyden, J.E., Webster, L.: 2002, Mount Wilson synoptic magnetic fields: Improved instrumentation, calibration, and analysis applied to the 14 July 2000 flare and to the evolution of the dipole field. *Astrophys. J. Suppl.* **139**, 259.

Wang, Y.M., Sheeley, N.R.: 1990a, Solar wind speed and coronal flux-tube expansion. *Astrophys. J.* **355**, 726.

Wang, Y.M., Sheeley, N.R.: 1990b, Magnetic flux transport and the sunspot-cycle evolution of coronal holes and their wind streams. *Astrophys. J.* **365**, 372.

Wenzel, K.P., Marsden, R.G., Page, D.E., Smith, E.J.: 1989, *Ulysses*: The first high-latitude heliospheric mission. *Adv. Space Res.* **9**(4), 25.